



# Structure-Preserved and Weakly Redundant Band Selection for Hyperspectral Imagery

Baijia Fu, Xudong Sun , *Student Member, IEEE*, Chuanyu Cui, Jiahua Zhang, and Xiaodi Shang , *Member, IEEE*

**Abstract**—In recent years, sparse self-representation has achieved remarkable success in hyperspectral band selection. However, the traditional sparse self-representation-based band selection methods tend to neglect the spatial distribution differences and spectral redundancy between heterogeneous regions. Consequently, the uniform band subset obtained cannot accurately express the key features of various region-specific objects. In this context, this article proposes the structure-preserved and weakly redundant (SPWR) band selection method for hyperspectral imagery (HSI). Initially, to preserve the spatial structure of HSI, heterogeneous regions are generated by superpixel segmentation. This process simulates the actual distribution of ground objects and captures the spectral feature differences from heterogeneous regions, thus adapting the sparse self-representation to diverse land cover types. Subsequently, given that the different objects between heterogeneous regions have different sensitive bands, a series of region-specific multimetric hypergraphs are constructed to more accurately express the multivariate adjacencies between bands for each region. Significantly, a new spectral similarity measure that integrates both the spectral distance and physical distance is elaborately utilized to group bands into various hypergraphs. Finally, a consensus matrix is designed to fuse multiple coefficient matrices carrying the local spatial-spectral information of HSI, thereby selecting the subset of bands for a unified characterization of HSI and achieving the complementarity of multiple regions. Extensive comparison experiments on four real-world datasets demonstrate that the proposed method SPWR can efficiently select representative bands and outperforms other comparison methods.

**Index Terms**—Region-specific multimetric hypergraph, sparse self-representation, spatial structure, unsupervised band selection, weakly redundancy.

Manuscript received 7 May 2024; revised 1 July 2024; accepted 2 July 2024. Date of publication 10 July 2024; date of current version 24 July 2024. This work was supported in part by Qingdao Natural Science Foundation under Grant 23-2-1-64-zyyd-jch, in part by China Postdoctoral Science Foundation under Grant 2023M731843, in part by the Postdoctoral Applied Research Foundation of Qingdao under Grant QDBSH20230101012, in part by the National Natural Science Foundation of China under Grant 42301380, and in part by the Science and Technology Support Plan for Youth Innovation of Colleges and Universities of Shandong Province of China under Grant 2023KJ232. (*Corresponding author: Xiaodi Shang.*)

Baijia Fu, Chuanyu Cui, and Xiaodi Shang are with the College of Computer Science and Technology, Qingdao University, Qingdao 266071, China (e-mail: fubaijia@qdu.edu.cn; cuichuanyu@qdu.edu.cn; shangxd@qdu.edu.cn).

Xudong Sun is with the School of Information Science and Technology, Dalian Maritime University, Dalian 116026, China (e-mail: sxd@dlnu.edu.cn).

Jiahua Zhang is with the Aerospace Information Research Institute, Chinese Academy of Sciences, Beijing 100094, China (e-mail: zhangjh@radi.ac.cn).

The source code is available at <https://github.com/fbj1212/SPWR.git>.  
Digital Object Identifier 10.1109/JSTARS.2024.3425906

## I. INTRODUCTION

**H**YPERSPECTRAL image (HSI) with hundreds of narrow spectral bands [1], [2], [3] can provide higher spectral resolution than RGB image, which is more conducive to the accurate identification of ground objects [4], [5]. However, the nanoscale spectral resolution of HSI also brings some challenges to data processing, such as high computational complexity and information redundancy leading to wasted storage space [6]. To solve these problems, dimensionality reduction is necessary [7], [8], [9].

Feature extraction and band selection are common techniques for dimensionality reduction [10]. Among them, feature extraction projects the original high-dimensional data into the low-dimensional space, which changes the physical properties of the original data and makes some key information corrupted [11], [12]. Contrarily, band selection selects the most discriminative subset of bands from HSI, which retains the information of the original data better without changing the physical properties of the bands, thus making the reduced data more interpretable and usable [13].

Band selection techniques can be broadly classified into supervised band selection and unsupervised band selection. Supervised band selection requires certain priori information, such as training samples and associated labels, and its development is somewhat hampered by the difficulty and expensive process of collecting sample labels [14], [15], [16]. In contrast, unsupervised band selection does not require explicit labels and solely uses unlabeled data to develop learning models. It provides a feasible solution for many band selection methods plagued by labels and makes it more convenient in application. In the past decade, the research on unsupervised band selection has developed rapidly, and the methods such as maximum-variance principal component analysis (MVPCA) [17], similarity-based ranking method [18] and Boltzmann entropy-based band selection (BE) [19] all have achieved good effects.

Due to the high redundancy of bands selected by the aforementioned ranking-based methods, it is challenging to further enhance performance. Consequently, some researchers have proposed clustering-based [20], [21] and subspace partition strategy-based band selection methods [22], [23], [24] in order to reduce the correlation of bands. For example, Jia et al. [25] introduced the enhanced fast density-peak-based clustering, which calculates the ranking score for each band by weighting the local density and intracluster distance. In consideration of the block diagonality of band similarity matrix, Li et al. [26]

proposed a block-diagonal representation learning model that utilizes a linear combination approach to assess the significance of bands within each subblock matrix. Furthermore, Wang et al. [27] developed a fast neighborhood grouping method, which employs a coarse-fine strategy to partition the HSI into multiple groups to obtain highly correlated and informative bands. Subsequently, Li et al. [24] presented a hyperspectral band selection method via difference between intergroups (DIG), which uses a grouping and sorting strategy to reasonably divide bands and obtain representative ones.

Recently, the application of sparse representation theory to the hyperspectral fields has been proven to be reasonable [28]. Sparse representation-based hyperspectral band selection [29], [30], [31] argues that arbitrary band vectors can be sparsely expanded in the feature space made up of band vectors of the entire HSI, which increases the interpretability of the model and significantly reduces data redundancy. For instance, Sun et al. [28] put forward a sparse self-representation model, which first incorporates sparse representation into hyperspectral band selection. After that, Sun et al. [29] proposed a dissimilarity weighted sparse self-representation method, which integrates the dissimilarity weighted regularization term with the sparse self-representation model and effectively reduces the redundancy of the band subset. To balance the error coefficient term and the sparse constraint term in the sparse self-representation-based band selection, Hu et al. [32] developed a multiobjective optimization-based band selection to produce a set of optimal solutions to construct the similarity matrix. In addition, Li et al. [33] proposed the multidictionary sparse representation band selection model, which subtly converts the band selection into the sparse solutions of each band vector with its matching dictionary, thereby significantly improving the computational efficiency. The aforementioned researchers have extended the functionality of the sparse self-representation-based band selection to some extent, but they ignore two important issues. First, the spatial information utilized insufficiently in the band selection process. Second, the adjacency relationship between the bands has not been fully considered.

The spectral features of ground objects in heterogeneous regions vary widely, so a uniform subset of bands cannot adequately summarize and express the essential features of the ground objects in all regions. Therefore, intending to fully utilize the spatial information to enhance the quality of the band subset, Jia et al. [34] proposed the multiscale superpixel-level group clustering framework for band selection based on the principle of complementarity of different superpixel segmentation methods and scale variability of different land cover types. Besides, Yang et al. [35] proposed the spectral-spatial band selection models (SML-AP and SRL-AP), which employ the superpixel segmentation technique to generate several superpixels and take the band criteria learned by relevant component analysis (RCA) as input for spectral clustering to select bands.

In response to the problem of inadequate utilization of band adjacency relationships, graphs can visually represent the adjacencies between data points, thereby effectively mining the manifold structure of the data. The representatives are the regularized sparse band selection via learned pairwise agreement [36], the

multiscale spectral features graph fusion [37], the scalable one-pass self-representation learning [38], the marginalized graph self-representation [39], and the graph-regularized subspace clustering [40], etc. However, all of the above use simple graphs constructed with pixels as vertices. On the one hand, sparse self-representation-based band selection that relies on the graph regularization term built from pixels for band selection only indirectly constrains the relevance of bands, which somewhat lessens the algorithm's effectiveness. On the other hand, the bands generally have complicated adjacencies to one another and exhibit regional specificity. In this case, the simple graph can only reflect the one-to-one correspondence among the bands instead of the one-to-many adjacent features.

Hypergraph can describe the adjacencies of multivariate associative objects through flexible hyperedges, thus preventing the loss of original information caused by forcibly converting multivariate relationships into binary relationships [41], [42]. However, hypergraph usually uses a single metric, resulting in inaccurate representation of local structure by their hyperedges, so a comprehensive evaluation indicator is essential. Moreover, the spectral features of ground objects exhibit considerable variation across regions, and thus the sensitive bands corresponding to different classes of ground objects are not consistent. Entropy rate superpixel (ERS) [43], [44], [45], [46] can delicately capture the spatial distribution characteristics of various types of ground objects, which helps to accurately delineate heterogeneous regions and extract the spatial structure of HSI.

Inspired by this, this article proposes the SPWR band selection model for hyperspectral imagery. First, ERS is used to capture the differences in spectral features of ground objects in heterogeneous regions. Second, from the spectral perspective, a series of multimetric hypergraphs are constructed to express the local multivariate adjacencies among bands in specific region. The band adjacency structure is rationalized by introducing the spectral similarity and spatial index of bands as indicator for comprehensive evaluation of band similarity, thereby guiding the optimization of sparse self-representation. Finally, a consensus matrix is designed to fuse the band reconstruction information of all heterogeneous regions to form a uniform subset of bands. Specifically, the contributions of this article are as follows:

- 1) SPWR can capture the differences of spectral features in heterogeneous regions and model the multivariate spectral-spatial adjacencies of bands within local area, which is ultimately used to constrain the optimization of sparse self-representation model and improve the quality of band subset.
- 2) The incorporation of spatial constraints in sparse self-representation ensures the maintenance of the manifold structure among the pixels in homogeneous regions while capturing the spectral differences between heterogeneous regions.
- 3) The designed comprehensive indicator effectively avoids the decision bias inherent in evaluating band similarity. The multimetric hypergraph helps to simulate the real multivariate correlation among bands, providing spectral constraint for model and reducing band redundancy.

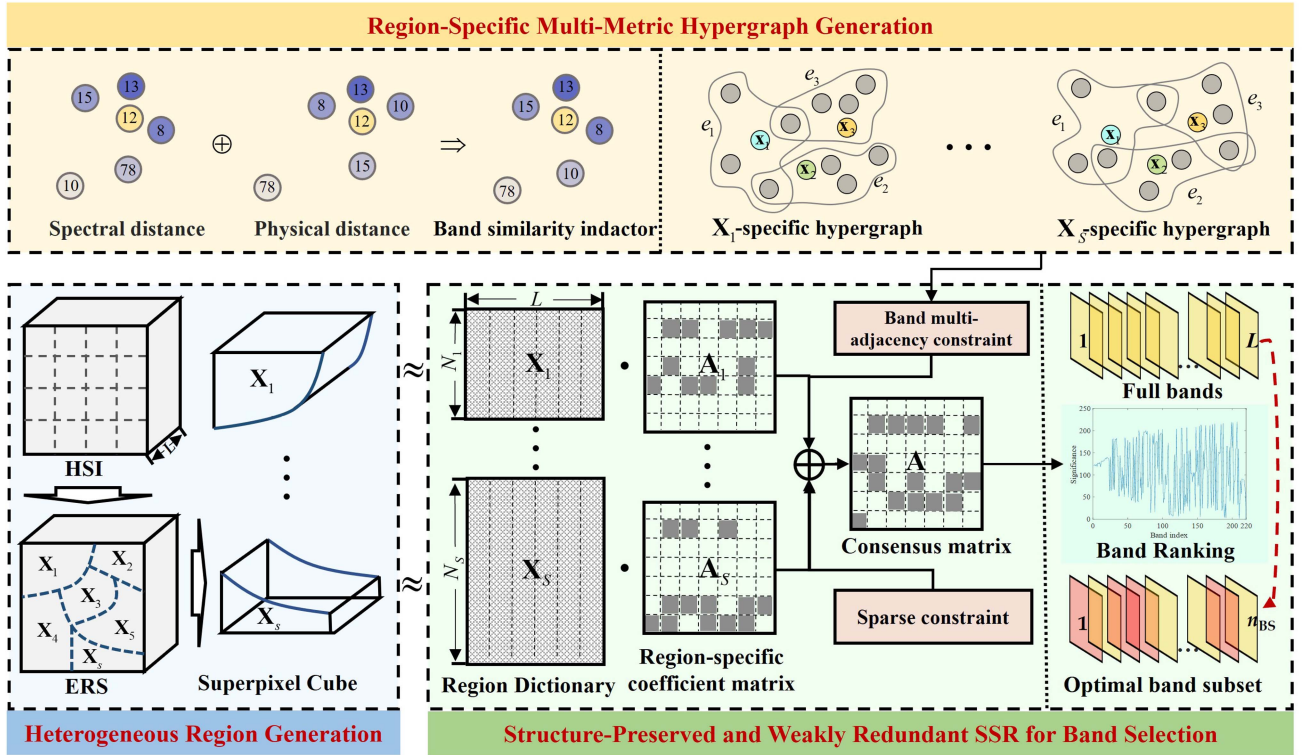


Fig. 1. Flowchart of SPWR. First, ERS segments the original HSI into multiple superpixel cubes to capture the differences in spectral features of various ground objects in heterogeneous regions. Second, spectral and physical distances are introduced as band similarity indicators to generate a series of multimetric hypergraphs that represent the multiadjacency between bands in a specific region. Finally, the band multiadjacency constraint, sparsity constraint, and consensus matrix are constructed to enable the sparse self-representation model to preserve image structural information and reduce band redundancy during the optimization process. Furthermore, the most representative bands are selected by band ranking.

The rest of this article is organized as follows: Section II introduces the proposed model SPWR. Section III presents the employed datasets and parameters setting in experiments, along with the analysis of results. Finally, Section IV concludes the article.

## II. PROPOSED METHOD

### A. Overview of SPWR Model

The distribution of ground objects in heterogeneous regions of HSI varies considerably, and the spectral features and sensitive bands are also different among regions. Consequently, it is not reasonable to represent the whole HSI with a uniform subset of bands. Therefore, this article proposes a novel method, named the structure-preserved and weakly redundant (SPWR), for hyperspectral band selection. As illustrated in Fig. 1, the HSI is first segmented into multiple regions by the superpixel segmentation technique ERS, thus exploring the spatial structure and mining the spectral feature differences of ground objects. Then, combining the spectral similarity and spatial index of bands, a series of multimetric hypergraphs are constructed to learn the region-specific band structures. Finally, the band multiadjacency constraint is applied to the sparse self-representation model, and a consensus matrix is introduced to integrate the spectral-spatial information of each region, thus reducing band redundancy and achieving the unification of the band subsets. In this way, SPWR

considers both the distribution feature of ground objects and the local structure of bands during the optimization process, which can effectively improve the quality of the band subset. The design and optimization process are described in the following section.

### B. Heterogeneous Region Generation

The 3-D HSI data cube is denoted as  $\mathbf{X} \in \mathbb{R}^{W \times H \times L}$  where the 2-D plane stores  $W \times H$  pixels, and  $L$  is the number of spectral bands. Actually, HSI covers many different kinds of ground objects, and the pixels that are spatially located next to each other, i.e., pixels in homogeneous regions, tend to have similar spectral features. In contrast, the spectral features of spatially distant pixels in heterogeneous regions exhibit large differences. Due to the different distribution of ground objects, it is reasonable that the corresponding characteristic bands should vary between heterogeneous regions. Accordingly, a superpixel segmentation technique, ERS, is employed in this model. Based on the high similarity of ground objects within the homogeneous region and significant differences between heterogeneous regions, ERS divides the original HSI into  $S$  nonoverlapping superpixel cubes  $\mathbf{X}_s$ ,  $1 \leq s \leq S$ , with similar spectral features to represent different coverages of the same types of ground objects. In this way, the sensitive bands of different ground objects are selected by type.

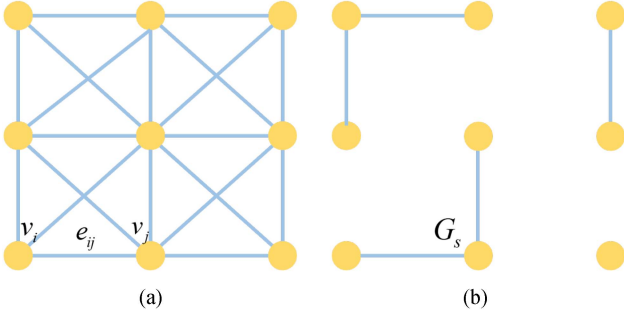


Fig. 2. Segmentation process of ERS. (a) Before segmentation. (b) After segmentation.

Specifically, ERS maps the first principal component of HSI to graph  $G(V, E)$ , where  $V$  is the set of vertices  $v_i$ . Besides,  $E$  is the set of edges  $e_{ij}$ , which connects pairwise pixels  $v_i$  and  $v_j$ . On this basis, the weight of  $e_{ij}$  can be represented as

$$w(e_{ij}) = \begin{cases} \exp\left(-\frac{\|v_i - v_j\|}{2\delta^2}\right), & v_i, v_j \in G_s \\ 0, & v_i \notin G_s \text{ or } v_j \notin G_s \end{cases} \quad (1)$$

where  $G_s$  represents the  $s$ th superpixel  $\mathbf{X}_s$  obtained by ERS, i.e.,  $G = \sum_{s=1}^S G_s$ .  $\delta = 1/K \sum_{v_j \in e_{ij}} \|v_i - v_j\|$  is a kernel parameter. Here, the similarity between pixels in the same region is calculated via  $\exp(-\|v_i - v_j\|/2\delta^2)$ , and the similarity between pixels in different regions is set to zero.

ERS aims to search a subset  $A$  from the edge set  $E$  so that graph  $\tilde{G}(V, A)$  contains all  $T$  connected subgraphs. In other words, the segmentation is finally achieved by removing some unnecessary edges from  $E$ . The objective function of ERS is

$$\max_A \text{Tr}\{H(A) + \beta B(A)\} \quad \text{s.t. } A \in E, N_A \geq T \quad (2)$$

Here,  $H(A)$  is the entropy rate of the random walk model on  $\tilde{G}(V, A)$ , which allows that the vertices on each cluster are compact and homogeneous. Besides,  $B(A)$  is an equilibrium term describing the cluster distribution to ensure that each cluster is similar in size. Moreover, the variable weight factor  $\beta$  is introduced to coordinate the proportional relationship between  $H(A)$  and  $B(A)$ , and  $N_A$  denotes the number of connected subgraphs in  $\tilde{G}(V, A)$ . Fig. 2 describes the process of ERS. As can be seen, the connectivity of the edges between clusters can be eliminated by the objective function, thus achieving the segmentation. Accordingly, the HSI  $\mathbf{X}$  can be rerepresented as  $\mathbf{X} = [\mathbf{X}_1, \mathbf{X}_2, \dots, \mathbf{X}_s, \dots, \mathbf{X}_S]$ .

### C. Region-Specific Multimetric Hypergraph Construction

In general, bands with similar spectra have comparable capabilities for reconstructing HSI. However, the traditional metric of band similarity is usually based on spectral distances alone. In fact, the bands of hyperspectral image are arranged sequentially. Due to the potential physical properties of the image, bands at different wavelengths should not be grouped in the same cluster, even if the spectra are extremely similar. Consequently, such a one-sided metric fails to accurately express the complex

neighborhood structure of bands, thus easily leading to biased decision-making.

Inspired by this, SPWR further considers the spectral information of a specific region on top of the spatial information extracted from the pixel perspective by ERS. In comparison to simple graphs, hypergraph can capture the high-order relationships among multiple data points, thus effectively modeling the spectral-spatial joint structure of HSI [42]. As a result, given that the spatial locations (wavelengths) of bands with similar spectral characteristics may not be adjacent, we devise a comprehensive evaluation indicator that combines the spectral similarity and physical characteristics (i.e., band index) between the bands, and construct the specific-region multimetric hypergraph to explore a more rational local structure that adequately expresses the adjacencies between bands both spectrally and spatially.

Accordingly, the multimetric hypergraph  $G_s^H = (V_s^H, E_s^H)$  for a specific region  $\mathbf{X}_s$  is constructed to form the complete hypergraph structure  $G^H = \{G_1^H, G_2^H, \dots, G_S^H\}$  of HSI. Here, the band vector  $\mathbf{b}_i$  is viewed as a vertex, and then  $V_s^H = \{\mathbf{b}_1, \mathbf{b}_2, \dots, \mathbf{b}_L\}$  can represent the vertex set consist of  $L$  bands of HSI. Moreover,  $E_s^H$  is the set of hyperedges  $e_i \in E_s^H$  corresponding to a hyperedge composed of the  $K$ -nearest neighbors of  $\mathbf{b}_i$ . On this basis, the weight  $w(e_i)$  of  $e_i$ , i.e., adjacent relationship, between  $K$  bands within the hyperedge  $e_i$  can be calculated as

$$w(e_i) = \sum_{\mathbf{b}_j \in e_i} \exp\left(\frac{\|f(\mathbf{b}_i) - f(\mathbf{b}_j)\|^2}{2\sigma^2}\right) \quad (3)$$

where  $\sigma$  is a kernel parameter, usually set to  $\sigma = 1/K \sum_{\mathbf{b}_j \in e_i} \|f(\mathbf{b}_i) - f(\mathbf{b}_j)\|$ . Besides,  $f(\mathbf{b}_i)$  denotes the integral function of  $\mathbf{b}_i$ , determined by  $\mathbf{b}_i$  and the remaining vertices in hyperedge  $e_i$  formed at the center of  $\mathbf{b}_i$ , i.e.,  $f(\mathbf{b}_i) = \sum_{\mathbf{b}_j \in e_i} \tilde{f}_{ij} \mathbf{b}_j$ . Since the remaining vertices in the hyperedge  $e_i$  have different affinities with  $\mathbf{b}_i$ ,  $\tilde{f}_{ij}$  is set to  $\tilde{f}_{ij} = f_{ij} / \sum_{\mathbf{b}_k \in e_i} f_{ik}$ . Here,  $f_{ij}$  combines both the spectral similarity  $f_{ij}^{\text{spe}}$  and the spatial proximity  $f_{ij}^{\text{spa}}$  of the bands, i.e.,  $f_{ij} = f_{ij}^{\text{spe}} \times f_{ij}^{\text{spa}}$  with  $f_{ij}^{\text{spe}}$  and  $f_{ij}^{\text{spa}}$  is expressed as

$$f_{ij}^{\text{spe}} = \exp\left(\frac{-\|\mathbf{b}_i - \mathbf{b}_j\|^2}{2\theta^2}\right) \quad (4)$$

$$f_{ij}^{\text{spa}} = \exp\left(\frac{-|I_{\mathbf{b}_i} - I_{\mathbf{b}_j}|^2}{2\omega^2}\right). \quad (5)$$

Here,  $\theta = 1/K \sum_{\mathbf{b}_j \in e_i} \|\mathbf{b}_i - \mathbf{b}_j\|$  and  $\omega = 1/K \sum_{\mathbf{b}_j \in e_i} |I_{\mathbf{b}_i} - I_{\mathbf{b}_j}|$  are equilibrium parameters.  $I_{\mathbf{b}_i}$  and  $I_{\mathbf{b}_j}$  represent the spatial index of  $\mathbf{b}_i$  and  $\mathbf{b}_j$ , respectively. Combining  $f_{ij}^{\text{spe}}$  and  $f_{ij}^{\text{spa}}$ ,  $f_{ij}$  not only considers the spectral information between adjacent bands in a hyperedge, but also further synthesizes the physical positional relationship between the wavelengths of the bands. This integration enables a more realistic modeling of the local-global correlation of the bands, enhances the accuracy of the similarity metric and reduces decision bias.

Finally, construct the incidence matrix  $\mathbf{H}_s$ , the weight matrix  $\mathbf{W}_s$ , the vertex-degree  $\mathbf{D}_s^v$ , and the hyperedge-degree matrix  $\mathbf{D}_s^e$

of each multimetric hypergraph  $G_s^H$  as follows:

$$\mathbf{H}_s(\mathbf{b}_j, e_i) = \begin{cases} 1, & \mathbf{b}_j \in e_i, \\ 0, & \text{otherwise} \end{cases} \quad (6)$$

$$\mathbf{W}_s = \text{diag}(w_s(e_1), w_s(e_2) \dots w_s(e_L)) \quad (7)$$

$$\mathbf{D}_s^v = \text{diag}(d_s^v(\mathbf{b}_1), d_s^v(\mathbf{b}_2) \dots d_s^v(\mathbf{b}_L)) \quad (8)$$

$$\mathbf{D}_s^e = \text{diag}(d_s^e(e_1), d_s^e(e_2) \dots d_s^e(e_L)) \quad (9)$$

where  $\text{diag}(\cdot)$  is the diagonal matrix,  $d_s^v(\mathbf{b}_j) = \sum_{i=1}^L w_s(e_i) h_s(\mathbf{b}_j, e_i)$  and  $d_s^e(e_i) = \sum_{j=1}^L h_s(\mathbf{b}_j, e_i)$ . At this point, the Laplacian matrix  $\mathbf{L}_s$  corresponding to  $G_s^H$  is given by

$$\mathbf{L}_s = \mathbf{I} - (\mathbf{D}_s^v)^{\frac{1}{2}} \mathbf{H}_s \mathbf{W}_s (\mathbf{D}_s^e)^{-1} \mathbf{H}_s^T (\mathbf{D}_s^v)^{\frac{1}{2}}. \quad (10)$$

Here,  $\mathbf{I}$  is the identity matrix.  $\mathbf{L}_s$  takes advantage of the distinctive spectral features of bands themselves and the spatial distance between the band sequences, which helps to reflect the adjacencies between bands in a more realistic manner and reduces redundancy.

#### D. Structure Preserved and Weakly Redundant Sparse Self-Representation for Band Selection

Sparse representation has been widely used in noise reduction, feature extraction, and pattern classification [29]. Sparse self-representation-based band selection holds that each band can be linearly represented by a few bands of HSI. Let  $\mathbf{X} = [\mathbf{b}_1, \mathbf{b}_2, \dots, \mathbf{b}_L]$  be a 2-D matrix of HSI composed of  $L$  bands with  $N$  pixels,  $\mathbf{b}_l = (x_1, x_2, \dots, x_N)^T$ ,  $1 \leq l \leq L$ , then the problem of band selection can be expressed as

$$\min_{\mathbf{A}} \|\mathbf{X} - \mathbf{X}\mathbf{A}\|_F^2 + \alpha \|\mathbf{A}\|_{2,1} \quad \text{s.t. } \mathbf{A} \geq 0, \text{diag}(\mathbf{A}) = \mathbf{0} \quad (11)$$

where  $\alpha$  denotes the regularization parameter,  $\|\cdot\|_{2,1}$  is the  $l_{2,1}$ -norm [23] that constrains the coefficient matrix  $\mathbf{A}$  with row sparsity in order to approximate the dataset using as few bands, i.e., dictionary columns, as possible.  $\|\cdot\|_F$  represents the Frobenius norm specified as  $\|\mathbf{A}\|_F = (\sum_{i=1}^L \sum_{j=1}^L |a_{ij}|^2)^{1/2}$ .  $\mathbf{A} \geq 0$  is used to ensure the nonnegative characteristics of the spectral response.  $\text{diag}(\mathbf{A}) = \mathbf{0}$  indicates that diagonal elements of  $\mathbf{A}$  are all zero, avoiding any band being represented by itself. Similarly, the objective function of each  $\mathbf{X}_s$  can be described as

$$\min_{\mathbf{A}_s} \|\mathbf{X}_s - \mathbf{X}_s \mathbf{A}_s\|_F^2 + \alpha \|\mathbf{A}_s\|_{2,1} \quad (12)$$

$$\text{s.t. } \mathbf{A}_s \geq 0, \text{diag}(\mathbf{A}_s) = \mathbf{0}.$$

Here,  $\mathbf{A}_s$  is the coefficient matrix of  $\mathbf{X}_s$ , indicating the contribution of the band in reconstructing  $\mathbf{X}_s$ . In order to synthetically evaluate the reconstruction capability of the bands for the whole image  $\mathbf{X}$ , a consensus matrix  $\mathbf{A}$  is designed to integrate all the coefficient matrices  $\mathbf{A}_s$  for  $\mathbf{X}_s$  to fuse all the local features as a whole, making the band selection more accurate. On this basis, the objective function is further defined as

$$\min_{\mathbf{A}_s, \mathbf{A}, w_s} \sum_{s=1}^S [\|\mathbf{X}_s - \mathbf{X}_s \mathbf{A}_s\|_F^2 + \lambda_1 w_s \|\mathbf{A}_s - \mathbf{A}\|_F^2] \quad (13)$$

$$+ \alpha \|\mathbf{A}\|_{2,1} \quad \text{s.t. } \mathbf{A}_s \geq 0, \text{diag}(\mathbf{A}_s) = \mathbf{0}$$

where  $\lambda_1$  is a regularization parameter and  $w_s$  is an adaptive equilibrium factor to ensure that  $\|\mathbf{A}_s - \mathbf{A}\|_F^2$  is overall minimized. Specifically, if  $\|\mathbf{A}_s - \mathbf{A}\|_F^2$  is large, then  $w_s$  should be reduced in order to minimize this term, and vice versa. Since the correlations such as the spectral similarity between bands and the similar reconstruction capability of the adjacent sequence bands cannot be captured in (13), based on the definition of the multimetric hypergraph in Section II-C, (13) can be further optimized as

$$\min_{\mathbf{A}_s, \mathbf{A}, w_s} \sum_{s=1}^S [LOSS(\mathbf{A}_s, w_s) + \lambda_2 \text{Tr}(\mathbf{A}_s^T \mathbf{L}_s \mathbf{A}_s)] \quad (14)$$

$$+ \alpha \|\mathbf{A}\|_{2,1} \quad \text{s.t. } \mathbf{A}_s \geq 0, \text{diag}(\mathbf{A}_s) = \mathbf{0}$$

where  $LOSS(\mathbf{A}_s, w_s) = \|\mathbf{X}_s - \mathbf{X}_s \mathbf{A}_s\|_F^2 + \lambda_1 w_s \|\mathbf{A}_s - \mathbf{A}\|_F^2$ .  $\lambda_2$  is a balance factor and  $\mathbf{L}_s$  represents the Laplacian matrix of region  $\mathbf{X}_s$ .  $\text{Tr}(\cdot)$  denotes the trace operator. Up to this point, based on preserving pixel-level spatial structure, the model further introduces the spectral-level band local-global constraints, which enables sparse self-representation to simultaneously consider multiple information in both spatial space and spectral space during the optimization process, and effectively reduce band redundancy. Subsequently, the iterative update algorithm [47] is adopted to solve (14) and  $\mathbf{A}$ ,  $\mathbf{A}_s$ , and  $w_s$  are optimized as follows:

- 1) Fix  $\mathbf{A}$  and  $w_s$ , optimize  $\mathbf{A}_s$ . The objective function of  $\mathbf{A}_s$  can be converted to

$$L(\mathbf{A}_s) = \sum_{s=1}^S [\|\mathbf{X}_s - \mathbf{X}_s \mathbf{A}_s\|_F^2 + \lambda_1 w_s \|\mathbf{A}_s - \mathbf{A}\|_F^2 + \lambda_2 \text{Tr}(\mathbf{A}_s^T \mathbf{L}_s \mathbf{A}_s)] \quad \text{s.t. } \mathbf{A}_s \geq 0, \text{diag}(\mathbf{A}_s) = \mathbf{0}. \quad (15)$$

By taking the derivative of (15) to zero, the update of  $\mathbf{A}_s$  is obtained as

$$\mathbf{A}_s^{(n+1)} = \frac{2\mathbf{X}_s^T \mathbf{X}_s + 2\lambda_1 \mathbf{A}_s^{(n)} w_s^{(n)}}{2\mathbf{X}_s^T \mathbf{X}_s + 2\lambda_1 w_s^{(n)} \mathbf{I} + \lambda_2 (\mathbf{L}_s^T + \mathbf{L}_s)}. \quad (16)$$

- 2) Fix  $\mathbf{A}_s$  and  $w_s$ , optimize  $\mathbf{A}$ . The objective function of  $\mathbf{A}$  can be simplified as

$$L(\mathbf{A}) = \sum_{s=1}^S \lambda_1 w_s \|\mathbf{A}_s - \mathbf{A}\|_F^2 + \alpha \|\mathbf{A}\|_{2,1}. \quad (17)$$

Let  $\mathbf{U} = \text{diag}(u_1, u_2, \dots, u_L)$  to be a  $L \times L$  diagonal matrix with  $u_i = 1/[2(\|\mathbf{a}_i\|_2^2 + \varsigma)^{1/2}]$ , where  $\varsigma$  is a minimal value to avoid zero-denominator. Then, (17) can be rewritten as

$$L(\mathbf{A}) = \sum_{s=1}^S \lambda_1 w_s \text{Tr}(\mathbf{A}_s - \mathbf{A})^T (\mathbf{A}_s - \mathbf{A}) + \alpha (\mathbf{U}^T + \mathbf{U}) \mathbf{A}. \quad (18)$$

By taking the derivative of (18) to zero and letting  $\sum_{s=1}^S w_s \mathbf{A}_s = \mathbf{F}$ ,  $\mathbf{A}$  can be updated as

$$\mathbf{A}^{(n+1)} = \frac{2\lambda_1 \mathbf{F}}{\alpha (\mathbf{U}^T + \mathbf{U}) + 2\lambda_1 \sum_{s=1}^S w_s^{(n)} \mathbf{I}}. \quad (19)$$

**Algorithm 1:** Framework of SPWR.

**INPUT:** HSI  $\mathbf{X}$ , the number of segmentations  $S$ , the number of neighbors in hyperedge  $K$ , the regularization parameter  $\lambda_1, \lambda_2, \alpha$ , and the number of selected bands  $n_{BS}$ ;

**OUTPUT:** the optimal band subset.

**1. Heterogeneous Region Generation:**

- 1.1 Extract the first principal component of HSI;
- 1.2 Use ERS to divide HSI into  $S$  heterogeneous regions, and rephrase the HSI as  $\mathbf{X} = [\mathbf{X}_1, \mathbf{X}_2, \dots, \mathbf{X}_s, \dots, \mathbf{X}_S]$ ;

**2. Region-Specific Multimetric Hypergraph Construction:**

- 2.1 Obtain the weight  $w(e_i)$  of hyperedge  $e_i$  via (3) based on the spectral similarity  $f^{spe}$  and the spatial proximity  $f^{spa}$  defined in (4) and (5);
- 2.2 Construct the incidence matrix  $\mathbf{H}_s$ , weight matrix  $\mathbf{W}_s$ , vertex-degree  $\mathbf{D}_s^v$ , and hyperedge-degree matrix  $\mathbf{D}_s^e$  of each multimetric hypergraph  $G_s^H$  by (6)–(9);
- 2.3 Calculate the Laplacian matrix  $\mathbf{L}_s$  via (10) and generate band multiadjacency constraint;

**3. Band Selection:**

- 3.1 Initialize  $n = 0$ ,  $\mathbf{A}^{(n)} = \mathbf{0}$ ,  $\mathbf{A}_s^{(n)} = \mathbf{0}$ ,  $w_s^{(n)} = 0$ ,  $\varepsilon = 1e^{-6}$  and  $n_{max} = 1e^2$ ;
- 3.2 Repeat
  - Update  $\mathbf{A}_s^{(n+1)}$  by (16);
  - Update  $\mathbf{A}^{(n+1)}$  by (19);
  - Update  $w_s^{(n+1)}$  by (20);
- 3.3 Until  $|\mathbf{A}^{(n+1)} - \mathbf{A}^{(n)}| < \varepsilon$  or  $n > n_{max}$ ;
- 3.4 Calculate the weight of the  $i$ th band via  $r_i = \|\mathbf{a}_i\|_2$ ;
- 3.5 Select optimal band subset of  $n_{BS}$  bands with respect to the  $n_{BS}$  largest  $r$ .

- 3) Fix  $\mathbf{A}_s$  and  $\mathbf{A}$ , optimize  $w_s$ . The optimization of  $w_s$  is given by

$$w_s^{(n+1)} = \frac{1}{2\|\mathbf{A}_s^{(n)} - \mathbf{A}^{(n)}\|_F}. \quad (20)$$

When the iteration reaches the maximum number of iterations  $n_{max}$  or  $\|\mathbf{A}^{(n+1)} - \mathbf{A}^{(n)}\|$  is less than the set threshold  $\varepsilon$ , the algorithm stops. At this point, each element  $a_{ij}$  in the learned consensus matrix  $\mathbf{A}$  represents the ability of band  $\mathbf{b}_i$  to reconstruct band  $\mathbf{b}_j$ , and the row vector  $\mathbf{a}_i$  can represent the contribution of  $\mathbf{b}_i$  in reconstructing all bands of the original data  $\mathbf{X}$ . Therefore, the total contribution of  $\mathbf{b}_i$  in reconstructing  $\mathbf{X}$  can be obtained by summing up the elements of  $\mathbf{a}_i$ . That is, the larger  $r_i = \|\mathbf{a}_i\|_2$ , the more important  $\mathbf{b}_i$  is. Therefore, the final subset of bands can be selected by sorting the total contribution of each band  $r_i$  in descending order for subsequent classification. Algorithm 1 provides the specific implementation process.

### III. EXPERIMENTS

In this section, we conduct extensive experiments on four public datasets to evaluate the performance of SPWR. First, the experimental setup, including the datasets, comparison methods, and evaluation metrics, is introduced. Second, the sensitivity of parameters is analyzed, and the classification performance

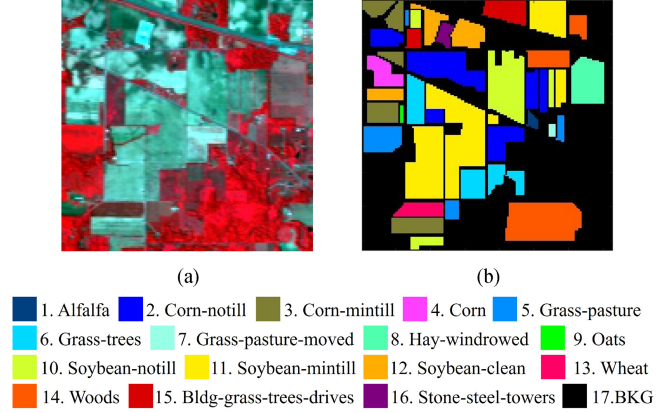


Fig. 3. Indian Pines dataset. (a) False-color image. (b) Ground truth.

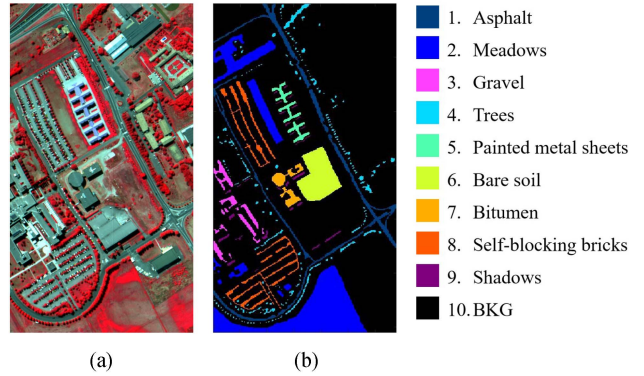


Fig. 4. University of Pavia dataset. (a) False-color image. (b) Ground truth.

of SPWR is compared with nine methods to demonstrate its reliability. Finally, we further discuss the computational and memory complexity.

#### A. Hyperspectral Datasets

1) *Indian Pines*: The Indian Pines dataset is sourced from the experimental area of Indiana, USA, and was captured by the Airborne Visible Infrared Imaging Spectrometer. It has 220 spectral bands with a range from 0.4 to 2.5  $\mu\text{m}$ . Its size is  $145 \times 145 \times 220$  with a total of 10 249 target pixels and 10 776 background pixels, including 16 different categories of land covers, such as corn-no-till, soybean-min-till, woods, etc. Fig. 3 shows its false-color image and ground truth, respectively.

2) *University of Pavia*: University of Pavia dataset was captured over the city of Pavia in northern Italy by the Reflective Optics Spectrographic Imaging System (ROSIS-03), a German airborne reflectance spectroscopy imager, with 115 bands. After removing 12 bands with noise and water absorption, the actual dataset used for training consisted of 103 bands and had a size of  $610 \times 340$  pixels, containing nine different categories of land covers, including grassland and bricks, etc. The dataset includes a total of 207 400 pixels, of which 42 776 are target pixels. The false-color image, and ground truth map of the University of Pavia are shown in Fig. 4(a) and (b), respectively.

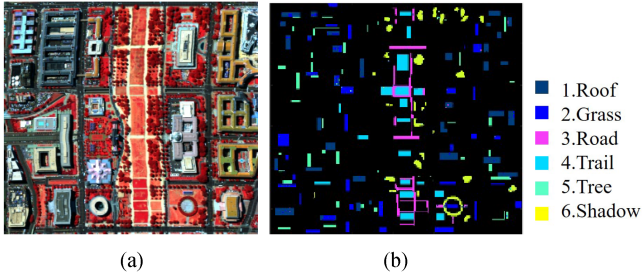


Fig. 5. Washington DC Mall dataset. (a) False-color image. (b) Ground truth.

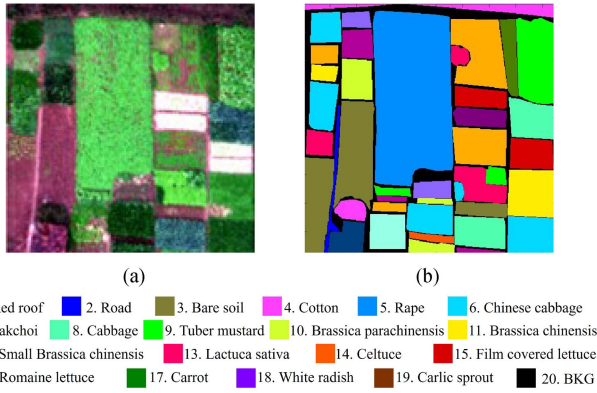


Fig. 6. Hong Hu dataset. (a) False-color image. (b) Ground truth.

3) *Washington DC Mall*: The Washington DC Mall dataset was captured by the hyperspectral digital imagery collection experiment sensor in Washington, United States. The size of this scene is  $280 \times 307$  pixels with 191 bands. It contains six different categories of land covers, including roof, grass, trees, road, trail, and shadow, with a total of 10 190 labeled samples. Fig. 5(a)–(b) displays the false-color image as well as ground truth of it, respectively.

4) *Hong Hu*: The Hong Hu dataset was extracted from the WHU-Hi-HongHu dataset and collected in 2017 in Honghu City, Hubei Province, China, using the DJI Matrice 600 Pro unmanned aerial vehicle platform equipped with Headwall Nano-Hyperspec imaging sensors. Its image size is  $441 \times 475$ , with 270 bands and 19 types of land covers. Fig. 6(a)–(b) shows its false-color image and ground truth.

### B. Comparators and Evaluation Metrics

Nine band selection methods are compared with the proposed approach. Their main steps are described as follows.

- 1) MVPCA [17]: It sorts the bands by a loading factors matrix, and selects the top-ranked bands to form the final band subset.
- 2) OCF [46]: It constructs an optimal clustering framework that adaptively selects a subset of bands while reducing the data dimensionality.
- 3) ASPS [23]: It maximizes the ratio of interclass distance to intraclass distance, and separates the HSI into subcubes,

choosing the least noisy band in each cube as the representative band.

- 4) GRSC [40]: It uses superpixel segmentation technology to extract potential features of regions and adaptively learns the similarity between potential features. Finally, a subspace clustering model is used to select valuable bands.
- 5) SOP-SRL [38]: It achieves band selection by dividing the original HSI into subsets, and introducing a graph regularization term to dynamically measure the local similarity between the selected bands.
- 6) EGCSR [48]: It introduces graph convolution into self-representation model to capture band structure information. Thus, generating a more robust self-representation coefficient matrix to select a subset of bands.
- 7) S<sup>4</sup>P [49]: It designs a multi-image fusion term to fuse similar graphs from different regions, which is used to capture the spatial structure in the self-representation space.
- 8) BSNNet-Conv [50]: It constructs a band attention module to calculate the weights of bands, and reconstructs the weighted HSI via an autoencoder, and finally prioritizes the bands.
- 9) DARecNet-BS [51]: It utilizes a self-attention mechanism to learn the global–local relationship between the spectral-spatial dimensions of the HSI and uses an autoencoder to reconstruct the HSI. Finally, it ranks the importance of each band and selects the top-ranked bands.

In the experiment, the support vector machine (SVM) [52] and  $k$ -nearest neighbor (KNN) [53] are chosen as the classifier to validate the effectiveness of our proposed model. For Indian Pines, University of Pavia, Washington DC Mall and Hong Hu datasets, we randomly selected 10%, 1%, 5%, and 1% of the samples as the training set, respectively, and the rest were used for testing. All band selection methods employ the same set of randomly selected training samples for classification, and all experiments are repeated five times and the average value is recorded for final comparison. Overall accuracy (OA), average accuracy (AA), and Kappa coefficient (Kappa) are used to assess the quality of the band subset [54]. Specifically, OA is the ratio of the number of correct predictions of the model to the total number. In addition, AA is defined as the average of all class accuracies [55], while the Kappa coefficient is a statistic widely used to measure the consistency of classification results, indicating the ratio of error reduction between classification and completely random classification [27]. The calculation of OA, AA, and Kappa are as follows:

$$OA = \frac{\sum_{i=1}^C \tilde{n}_i}{\sum_{i=1}^C n_i} \quad (21)$$

$$AA = \frac{1}{C} \sum_{i=1}^C \frac{\tilde{n}_i}{n_i} \quad (22)$$

$$Kappa = \frac{p_o - p_e}{1 - p_e} \quad (23)$$

Here,  $C$  represents the number of types of ground objects in the HSI.  $n_i$  is the total number of pixels in class  $i$ , and  $\tilde{n}_i$  donates the number of pixels in class  $i$  that have been correctly classified.  $p_o$

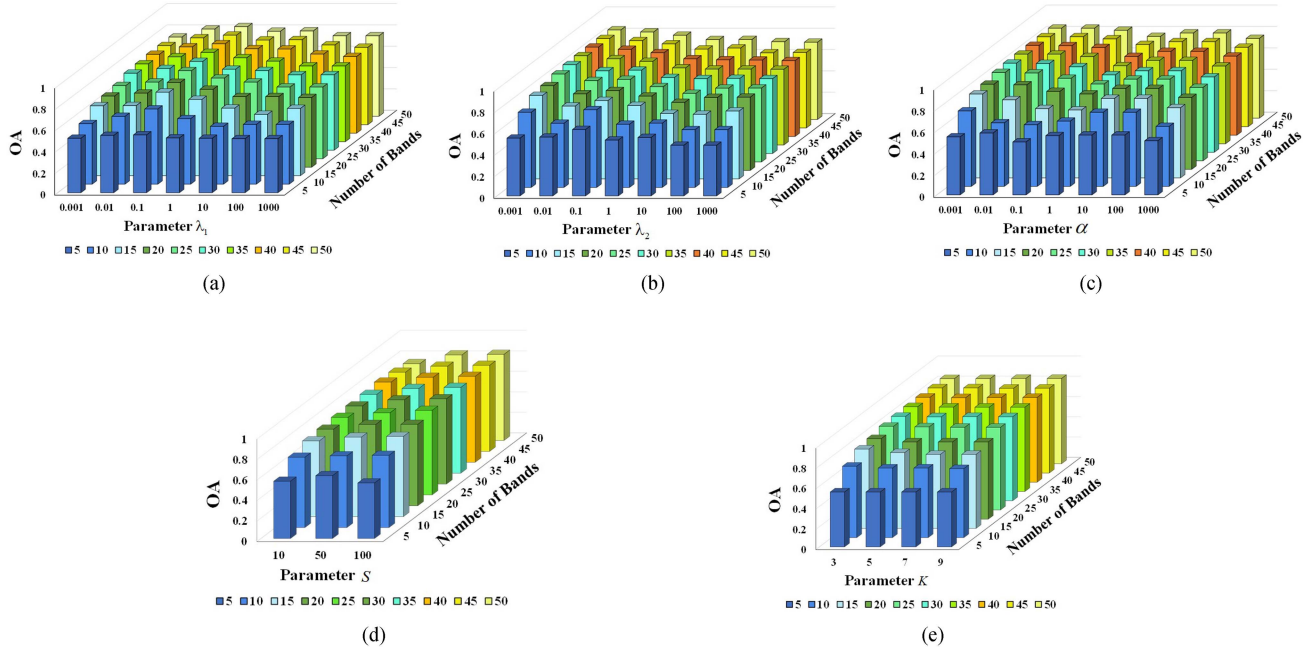


Fig. 7. Sensitivity test of parameters in terms of OA by SVM on the Indian Pines dataset. (a) Regularization parameter  $\lambda_1$ . (b) Regularization parameter  $\lambda_2$ . (c) Regularization parameter  $\alpha$ . (d) Number of segmentations  $S$ . (e) Number of nearest neighbors  $K$ .

TABLE I  
OPTIMAL PARAMETERS

Dataset	$S$	$K$	$\lambda_1$	$\lambda_2$	$\alpha$
Indian Pines	100	3	$1e^{-1}$	$1e^{-3}$	$1e^{-3}$
University of Pavia	10	3	$1e^{-1}$	$1e^{-3}$	$1e^{-3}$
Washington DC Mall	50	3	$1e^2$	$1e^{-1}$	$1e^{-2}$
Hong Hu	10	3	1	$1e^{-1}$	1

is the relatively observed agreement and  $p_e$  is the hypothetical probability of chance agreement.

### C. Parameters Setup and Sensitivity Analysis

SPWR contains a total of five parameters  $S$ ,  $K$ ,  $\lambda_1$ ,  $\lambda_2$ , and  $\alpha$ . Concretely, the number of segmentations  $S$  varies within  $\{10, 50, 100\}$  and the number of neighbors in hyperedge  $K$  is chosen from  $\{3, 5, 7, 9\}$ . Besides, the regularization parameters  $\lambda_1$ ,  $\lambda_2$ , and  $\alpha$  are chosen from  $\{1e^{-3}, 1e^{-2}, 1e^{-1}, 1, 1e^1, 1e^2, 1e^3\}$ . In the experiments, voting is employed to select the optimal parameters. The set of parameters with the most occurrences is selected as the optimal parameters under the different numbers of selected bands ranging from 5 to 50 with step 5. The optimal parameters are listed in Table I. Notably, although they do not reflect the best performance of SPWR, they still work well and improve the usability of SPWR on a variety of datasets.

Using the Indian Pines dataset as an example, we analyze the effect of each parameter on SPWR based on the SVM classification results of a subset of bands. The optimal values of parameters  $S$ ,  $K$ ,  $\lambda_1$ ,  $\lambda_2$ , and  $\alpha$  are set to 100, 3,  $1e^{-1}$ ,  $1e^{-3}$ ,  $1e^{-1}$ , and  $1e^{-1}$ , respectively. The univariate form is used to verify the effect of a parameter while keeping the other

parameters at their default values. Fig. 7 illustrates the variation of OA values for different values of parameters at different numbers of bands.

Fig. 7 demonstrates that the performance of SPWR remains stable within the local parameter range of  $S$ . Specifically, excellent and similar classification results are obtained for  $S=50$  and  $S=100$  in all bands. Regarding parameter  $K$ , the classification results are almost consistent across different values  $n_{BS}$ . When  $n_{BS}$  is small (e.g., 10–30), SPWR’s performance is more sensitive to changes in parameters  $\lambda_1$ . However, as  $n_{BS}$  increases, this gap gradually decreases. Moreover, the dimensionality reduction effect of the hypergraph and sparse terms is controlled by  $\lambda_2$  and  $\alpha$ , and is more effective when the values of these terms are small. However, their effectiveness deteriorates as the values increase.

### D. Results Analysis

To validate the effectiveness of SPWR, the experiments compare SPWR with nine comparison methods using two classifiers on four datasets. The OA, AA, and Kappa values obtained by the band subset selected by the various band selection methods are depicted in Figs. 8–10, respectively. In addition, the standard deviation of five runs under each number of bands is also calculated to demonstrate the stability of those methods.

As illustrated in Fig. 8, MVPCA performs poorly across all datasets. OCF performed well on the Hong Hu dataset, but poorly on the first three. ASPS and GRSC are only moderate. In addition, the three sparse representation-based band selection methods SOP-SRL, EGCSR, and  $S^4P$  also fail to achieve satisfactory performance on all datasets. For example, SOP-SRL performs relatively poorly on the first two datasets and its OA



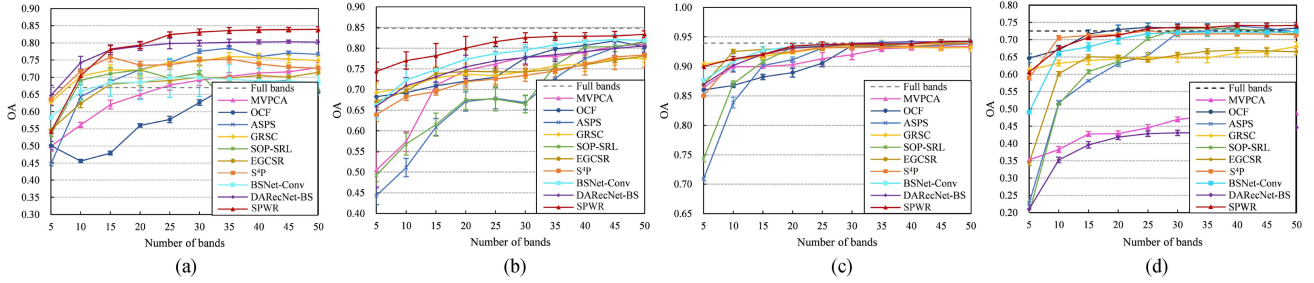


Fig. 8. OA values of SVM classifier with various band selection approaches on the four datasets. (a) Indian Pines. (b) University of Pavia. (c) Washington DC Mall. (d) Hong Hu.

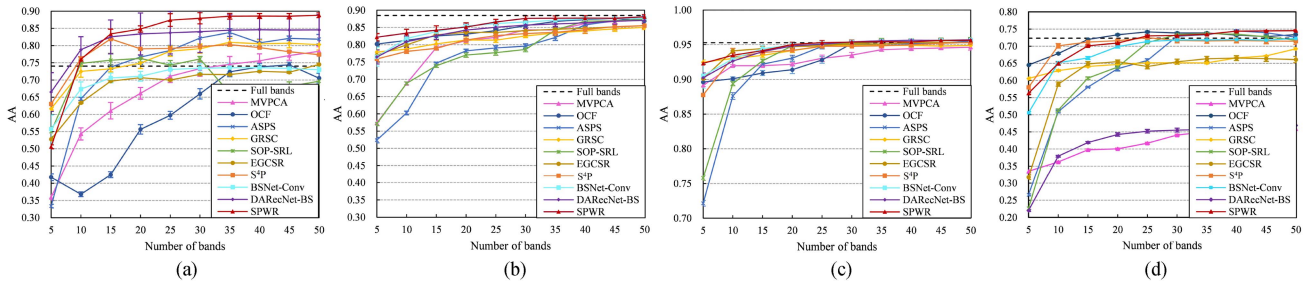


Fig. 9. AA values of SVM classifier with various band selection approaches on the four datasets. (a) Indian Pines. (b) University of Pavia. (c) Washington DC Mall. (d) Hong Hu.

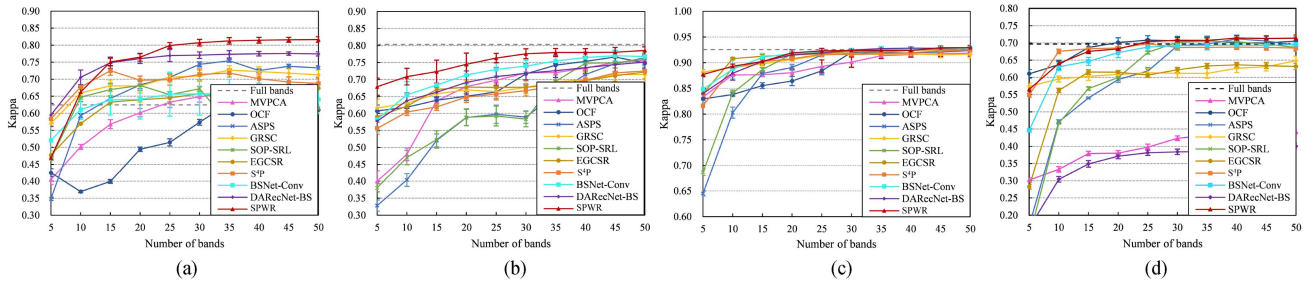


Fig. 10. Kappa values of SVM classifier with various band selection approaches on the four datasets. (a) Indian Pines. (b) University of Pavia. (c) Washington DC Mall. (d) Hong Hu.

values are in the middle to lower range. Also, for the Washington DC Mall and Hong Hu datasets, the performance of SOP-SRL in the first half is unsatisfactory. However, as the number of bands increases, the performance of SOP-SRL gradually stabilizes and surpasses most methods. BSNet-Conv performs mediocly on the Indian Pines and Hong Hu datasets, but excels on the University of Pavia dataset. When  $n_{BS}$  exceeds 10, its OA consistently surpasses most comparative methods. DARecNet-BS does a good job on the first three datasets, but it performs poorly on the last dataset.

On the Indian Pines dataset, when  $n_{BS}$  exceeds 15, the OA of SPWR tends to stabilize and gradually surpasses all comparative methods. For the second dataset, SPWR outperforms other comparative methods in the full band and holds the top spot. On the third dataset, with 20 bands as the cutoff point, the classification results of the subset of bands selected by SPWR

transcend most of the comparative methods in the first half of the period, and gradually stabilize, while still maintaining the leading position and even surpassing the full-band in the second half. On the last dataset, with 30 bands as the dividing point, the value of SPWR is only lower than OCF and S<sup>4</sup>P in most bands in the first half. However, when the number of bands is greater than 30, the value of SPWR gradually surpasses all comparison methods and ranks first.

It is well known that OA is more favorable for evaluating the overall classification performance, while AA and Kappa values are more suitable for accessing how well large and small classes are classified. As can be clearly observed from Figs. 9 and 10, the AA and Kappa values of SPWR stand out on the first three datasets. Especially, on the University of Pavia dataset, the Kappa values of SPWR are higher than the others in most bands. On the Hong Hu dataset, SPWR is only lower than

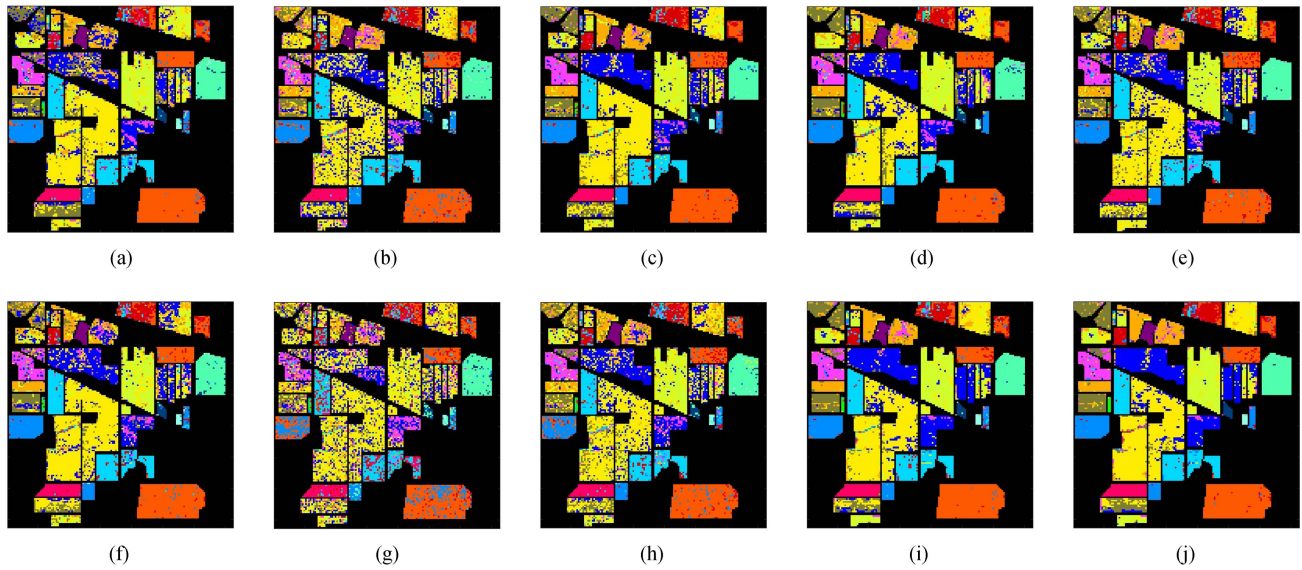


Fig. 11. Classification maps of Indian Pines with SVM classifier using 10% of training samples at 25 bands. (a) MVPCA (68.69%). (b) OCF (58.06%). (c) ASPS (75.56%). (d) GRSC (75.62%). (e) SOP-SRL (70.71%). (f) EGCSR (69.03%). (g)  $S^4P$  (73.63%). (h) BSNet-Conv (63.75%). (i) DARecNet-BS (81.26%). (j) SPWR (83.79%).

OCF and  $S^4P$  in most bands, but it is worth noting that when the number of bands is greater than 40, the value of SPWR begins to surpass all comparison methods and is in a leading position. The above experimental results prove that the band subsets selected by SPWR have good classification results on both large and small classes, which helps to improve the classification performance across the board.

In order to provide a more understandable overview of the performance of each method, Figs. 11–14 illustrate the classification results and accompanying OA values for each method on four datasets with 25 bands, respectively. It can be seen that SPWR obtains the highest classification accuracy on the first three datasets, which are 83.79%, 82.96%, and 94.14% in turn. For the Indian Pines dataset, there is a large disparity in the classification results of the various methods, with SPWR pulling ahead of the worst OCF by over 25.73%. In addition, on the second dataset, only the OA value of SPWR exceeds 80%, and its classification accuracy is 3.65% higher than the second-place BSNet-Conv. The classification performance of these methods on the Washington DC Mall dataset is comparable, but it is worth noting that SPWR is still the best. On the last dataset, SPWR lagged behind OCF by only 1.43%, ranking second.

To further test the stability of SPWR, Fig. 15 displays the average value of OA (AOA) of the compared methods on the four datasets to compare the overall performance of each method at the different number of bands. It shows that SPWR has the highest AOA values on the first three datasets. Especially on the University of Pavia dataset, the AOA value of SPWR is significantly higher than the other methods. Fig. 15(a) shows that multiple comparison methods are poorly stabilized on this dataset, but SPWR still performs excellently with the highest AOA value. From Fig. 15(b) and (c), the classification of band subsets obtained by each method is relatively consistent on these

two datasets as compared to the Indian Pines dataset. SPWR both ranks first, pulling away from the second-place BSNet-Conv by 3.06% and 0.2%, respectively. It can be seen from Fig. 15(d) that only the AOA values of SPWR, OCF, and  $S^4P$  exceed 70%, and SPWR lags behind OCF by only 0.3%.

In addition, we incorporated a KNN classifier to reinforce the effectiveness of SPWR. Fig. 16 shows the KNN classification results for the band subsets selected by each method across different numbers of bands. Among them, the parameters of SPWR used here are the optimal parameters corresponding to the four datasets under the SVM classifier, in order to demonstrate the stability of SPWR. Fig. 16 reveals that SPWR performs excellently despite not always achieving the best results with the KNN classifier.

Furthermore, Fig. 17 also illustrates the AOA values of the KNN classifier with various band selection methods across four datasets. The results indicate that SPWR performs best on Indian Pines and Washington DC Mall datasets. On the University of Pavia dataset, SPWR lags behind EGCSR and OCF, yet the discrepancy with the second-ranked OCF is merely 0.19%. Furthermore, SPWR ranks second on the Hong Hu dataset, with an AOA value 1.02% below  $S^4P$ . It is worth noting that EGCSR and OCF are unstable, as they are both downstream on the Indian Pines dataset, while  $S^4P$  does not perform well on any of the first three datasets. The above also demonstrates the validity of the proposed model.

The distribution of bands is an important indicator to evaluate the quality of the band subset. In general, bands with a narrow distribution are more redundant and contain less information, while bands with a wider distribution are more informative [23]. Accordingly, Table II displays the subset of 25 bands selected by SPWR for the four datasets. It is evident that our proposed method can select a wide range of bands for all four

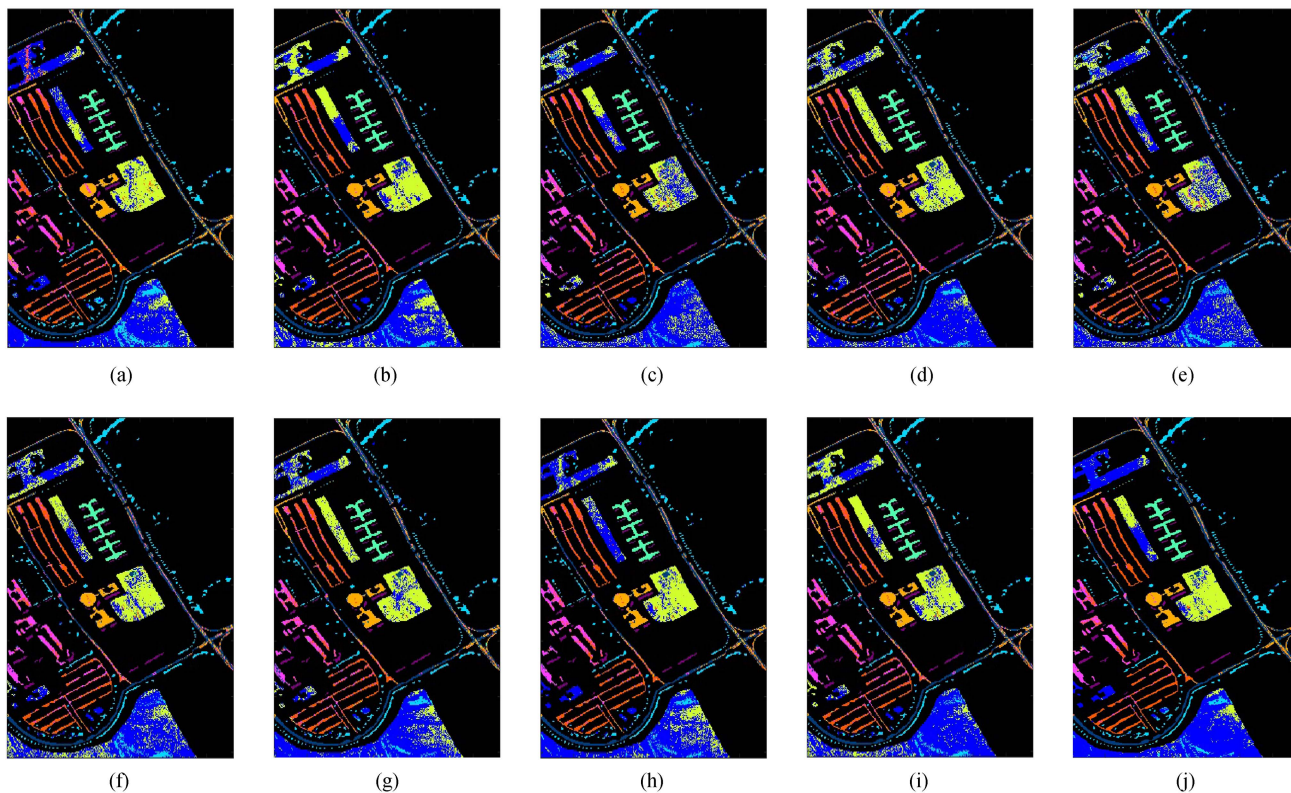


Fig. 12. Classification maps of University of Pavia with SVM classifier using 1% training samples at 25 bands. (a) MVPCA (77.12%). (b) OCF (73.81%). (c) ASPS (77.38%). (d) GRSC (73.66%). (e) SOP-SRL (71.36%). (f) EGCSR (74.29%). (g)  $S^4P$  (72.54%). (h) BSNet-Conv (79.31%). (i) DARecNet-BS (73.75%). (j) SPWR (82.96%).

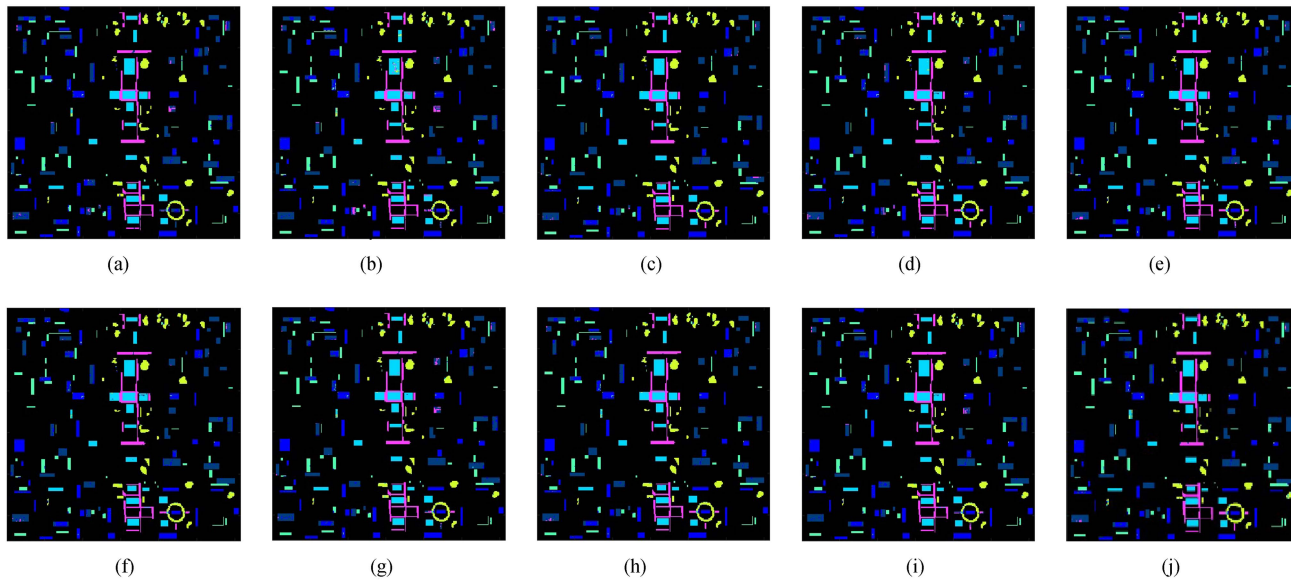


Fig. 13. Classification maps of Washington DC Mall with SVM classifier using 5% training samples at 25 bands. (a) MVPCA (89.23%). (b) OCF (90.72%). (c) ASPS (93.41%). (d) GRSC (92.91%). (e) SOP-SRL (93.55%). (f) EGCSR (93.29%). (g)  $S^4P$  (93.20%). (h) BSNet-Conv (93.94%). (i) DARecNet-BS (93.21%). (j) SPWR (94.14%).

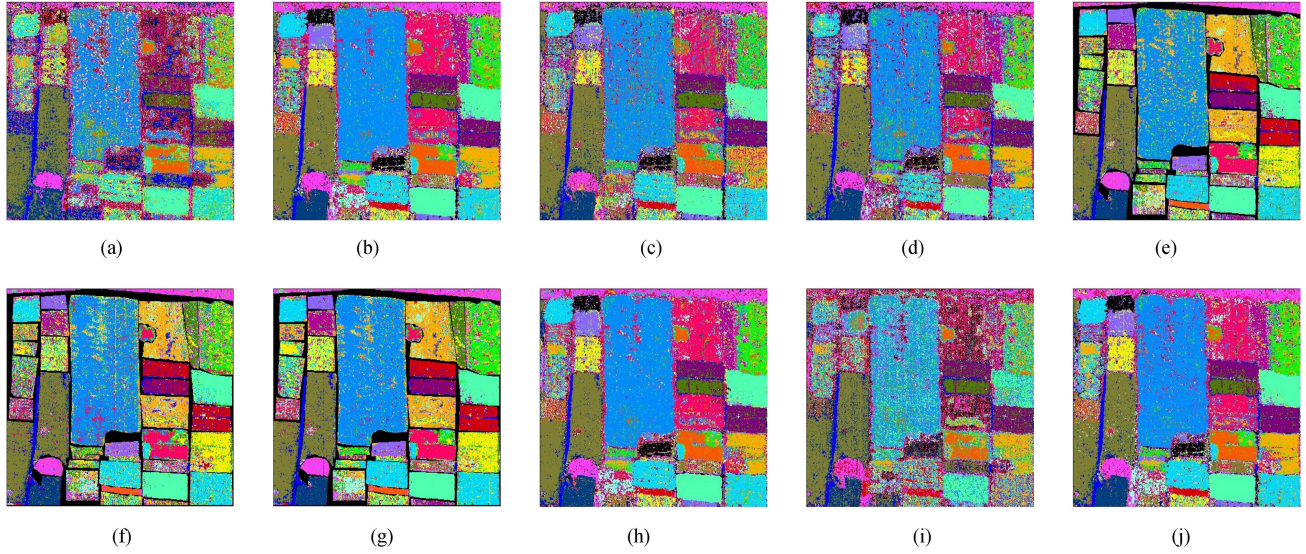


Fig. 14. Classification maps of Hong Hu with SVM classifier using 1% training samples at 25 bands. (a) MVPCA (44.59%). (b) OCF (75.45%). (c) ASPS (67.08%). (d) GRSC (66.01%). (e) SOP-SRL (70.92%). (f) EGCSR (64.18%). (g) S<sup>4</sup>P (72.62%). (h) BSNet-Conv (73.56%). (i) DARecNet-BS (43.75%). (j) SPWR (74.02%).

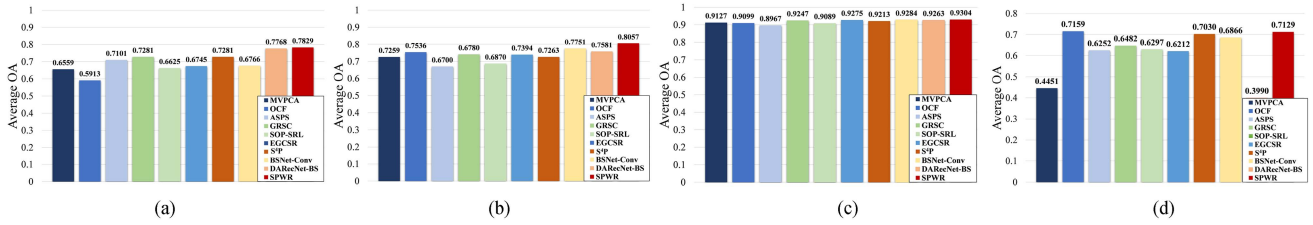


Fig. 15. Average OA values of SVM classifier with various band selection approaches on the four datasets. (a) Indian Pines. (b) University of Pavia. (c) Washington DC Mall. (d) Hong Hu.

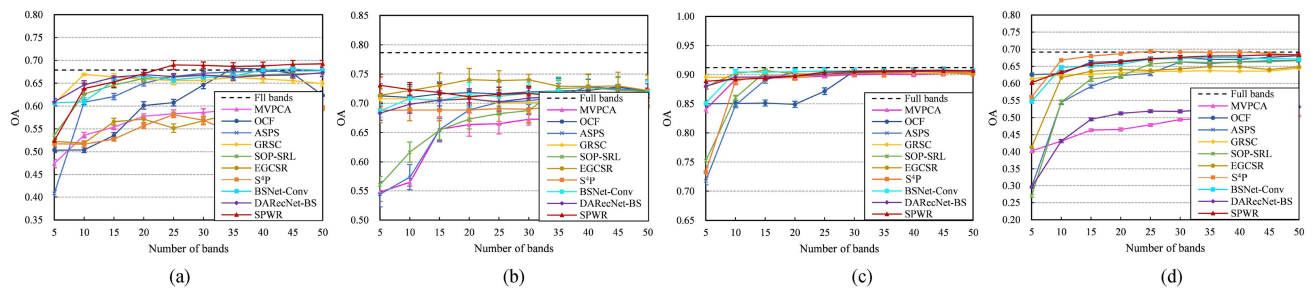


Fig. 16. OA values of KNN classifier with various band selection approaches on the four datasets. (a) Indian Pines. (b) University of Pavia. (c) Washington DC Mall. (d) Hong Hu.

TABLE II  
BAND SUBSETS SELECTED BY SPWR FOR THE FOUR DATASETS

Datasets	Band Subset
Indian Pines	92 9 8 7 10 37 38 99 52 122 53 181 36 6 182 123 98 183 124 121 100 28 120 180 132
University of Pavia	83 72 86 85 41 82 77 70 78 39 73 65 38 57 43 97 96 67 99 58 61 63 40 69 29
Washington DC Mall	51 80 95 79 59 191 61 184 69 49 52 111 116 181 175 94 50 4 135 68 177 26 93 7 67
Hong Hu	135 162 138 98 167 163 128 141 85 140 126 68 10 88 4 125 136 143 113 164 25 133 71 72 22

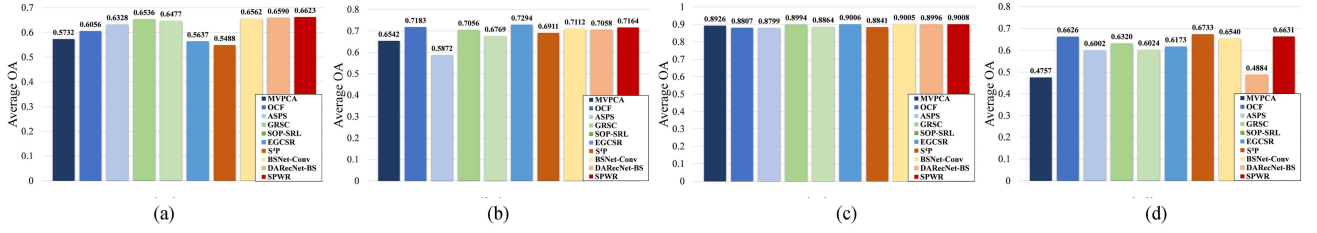


Fig. 17. Average OA values of KNN classifier with various band selection approaches on the four datasets. (a) Indian Pines. (b) University of Pavia. (c) Washington DC Mall. (d) Hong Hu.

TABLE III  
RUNTIME (S) OF EIGHT BS METHODS FOR FOUR DATASETS

Dataset	Indian Pines	University of Pavia	Washington DC Mall	Hong Hu
MVPCA	0.03	0.24	0.10	3.67
OCF	0.36	0.73	0.66	1.61
ASPS	2.01	1.03	0.90	3.80
GRSC	9.13	5.77	6.48	20.70
SOP-SRL	0.32	0.07	0.18	1.21
EGCSR	0.37	0.65	2.02	8.98
S <sup>4</sup> P	3.36	19.20	8.93	42.00
BSNet-Conv	642.36	1529.71	573.90	>5h
DARecNet-BS	814.92	1947.38	810.18	>8h
SPWR	24.05	33.38	59.94	246.77

datasets. The band ranges for the Indian Pines, University of Pavia, Washington DC Mall, and Hong Hu datasets are 6–183, 4–99, 4–191, and 4–167, respectively. Besides, the classification maps (Figs. 11–14) of 25 bands for the four datasets show that, except the Hong Hu dataset, the classification accuracy of the band subset obtained by SPWR is higher than that of other comparison methods, further confirming the higher quality of the selected bands.

In conclusion, the above experimental results demonstrate that the proposed method adopts the superpixel segmentation technique and multiple metrics to construct the local spectral-spatial hypergraph, which can effectively capture the spatial information at the pixel level, more realistically portray the correlation between bands, and enhance the quality of band subsets so that to improve the classification result.

### E. Complexity Analysis

1) *Time Complexity*: The contribution of the time complexity of SPWR mainly comes from the calculation of the objective function and two main variables,  $\mathbf{A}$  and  $\mathbf{A}_s$  in the iterative process. ERS divides the hyperspectral image  $\mathbf{X}$  into  $S$  nonoverlapping superpixels  $\mathbf{X}_s$  with  $N_s$  pixels,  $1 \leq s \leq S$ . At each iteration of SPWR, the calculation of coefficients matrix  $\mathbf{A}_s$  for each superpixel  $\mathbf{X}_s$  takes  $O(N_s L^2 + L^2)$  with the number of bands  $L$ , so calculating all coefficient matrices requires the cost of  $O(\sum_{s=1}^S (N_s L^2 + L^2))$ . In addition, the time cost for updating consensus matrix  $\mathbf{A}$  is  $O(\sum_{s=1}^S L^2)$ , and updating the objective function requires  $O(\sum_{s=1}^S (N_s L^2 + L^3) + L^3)$ . In general, the overall time complexity of SPWR is  $O(T(\sum_{s=1}^S (N_s L^2 + L^3) + L^3))$ , where  $T$  denotes the number of iterations. Since  $N_s$  is less than the total number of pixels  $N$ , the time complexity can

TABLE IV  
TIME COMPLEXITY OF COMPARISON METHODS

Method	Time Complexity
MVPCA	$O(L^2 N + L^2 \log L)$
OCF	$O(L^2 N + L^3 + L^2 K)$
ASPS	$O(L^2 W H + S Y^2)$
GRSC	$O(W H \times \log(W H) + L M^2 + (S + 1) L^3 + (L^3 + S d k) T)$
SOP-SRL	$O(\sum_{t=1}^m T_2 T_1 t^3)$ or $O(\sum_{t=1}^m T_2 T_1 t n_t^2)$
EGCSR	$O(L^2 N + L^2 \log L)$
S <sup>4</sup> P	$O(L^2 W H + W H \log(W H) + T(L^2 N))$
SPWR	$O(T(\sum_{s=1}^S (N T^2 + L^3) + L^3))$

also be re-expressed as  $O(T(\sum_{s=1}^S (N L^2 + L^3) + L^3))$ . The time complexity of various band selection methods is listed in Table III. Two deep learning-based methods, BSNet-Conv and DARecNet-BS, are not listed here because they typically run longer than machine learning-based methods due to their long training time and large number of computations.

For an intuitive time comparison, Table IV lists the runtime (s) of various band selection methods. The machine learning-based band selection methods were executed on a computer equipped with Intel Core i7-11700 K, 3.60 GHZ base frequency CPU, and 64 GB memory, and implemented using MATLAB with version 2022a. The deep learning-based band selection methods were executed on a computer equipped with Nvidia RTX4090 GPU and implemented using the PyTorch framework based on CDUA 10.7. It is evident that the runtime of deep learning-based band selection methods BSNet-Conv and DARecNet-BS is significantly longer than that of machine learning. Therefore, the analysis of the runtime of deep learning methods is excluded. It should be noted that MVPCA, SOP-SRL, EGCSR, and the proposed method SPWR can generate the priority sequence

of all bands in a single execution, and the band subset can be obtained according to the required number of bands. In contrast, several comparative band selection methods, such as OCF, ASPS, GRSC, and S<sup>4</sup>P, require re-execution when the number of bands changes. Therefore, even though SPWR has a longer execution time, its results are comprehensive and can promptly meet the demand for comparison of different band numbers.

2) *Memory Complexity*: The memory consumption of SPWR mainly comes from the storage of several main variables,  $\mathbf{X}_s$ ,  $\mathbf{A}_s$ ,  $\mathbf{L}_s$ ,  $\mathbf{X}$ , and  $\mathbf{A}$ . In particular, it takes  $O(\sum_{s=1}^S N_s L)$  to store superpixels  $\mathbf{X}_s$ . Moreover, the memory cost of coefficients matrix  $\mathbf{A}_s$  and Laplacian matrix  $\mathbf{L}_s$  both are  $O(\sum_{s=1}^S L^2)$ . For the matrices  $\mathbf{X}$  and  $\mathbf{A}$ , the storage requirements are  $O(NL)$  and  $O(L^2)$ , respectively. Therefore, the whole memory consumption of SPWR is  $O(\sum_{s=1}^S (N_s L + L^2) + NL + L^2)$ .

#### IV. CONCLUSION

In this article, we propose a SPWR model for unsupervised hyperspectral band selection that fully takes into account the differences in spectral features of heterogeneous regions. It utilizes the superpixel segmentation technique ERS for generating homogeneous regions to capture the spatial structure of local views, while constructing a series of region-specific multimetric hypergraphs to obtain the interband multivariate adjacencies of the local views, thus improving the overall performance of the sparse self-representation model. The results of SVM and KNN classification on four publicly available datasets demonstrate that SPWR is stable and effective, outperforming other compared methods.

Currently, there are more experimental parameters of SPWR, which restricts the model's applicability in practical settings. In the future, we will work on designing an automated parameter-seeking algorithm, thereby enhancing the model's usability.

#### REFERENCES

- [1] D. Wang, L. Zhuang, L. Gao, X. Sun, X. Zhao, and A. Plaza, "Sliding dual-window-inspired reconstruction network for hyperspectral anomaly detection," *IEEE Trans. Geosci. Remote Sens.*, vol. 62, 2024, Art. no. 5504115.
- [2] A. F. H. Goetz et al., "Imaging spectrometry for earth remote sensing," *Science*, vol. 228, no. 4704, pp. 1147–1153, Jun. 1985.
- [3] R. O. Green et al., "Imaging spectroscopy and the airborne visible/infrared imaging spectrometer," *Remote Sens. Environ.*, vol. 65, no. 3, pp. 227–248, Sep. 1998.
- [4] D. Wang, L. Zhuang, L. Gao, X. Sun, M. Huang, and A. J. Plaza, "PDB-Net: Pixel-shuffle downsampling blind-spot reconstruction network for hyperspectral anomaly detection," *IEEE Trans. Geosci. Remote Sens.*, vol. 61, 2023, Art. no. 5511914.
- [5] B. Zhang, X. Sun, L. Gao, and L. Yang, "Endmember extraction of hyperspectral remote sensing images based on the ant colony optimization (ACO) algorithm," *IEEE Trans. Geosci. Remote Sens.*, vol. 49, no. 7, pp. 2635–2646, Jul. 2011.
- [6] H. Huang, G. Shi, H. He, Y. Duan, and F. Luo, "Dimensionality reduction of hyperspectral imagery based on spatial-spectral manifold learning," *IEEE Trans. Cybern.*, vol. 50, no. 6, pp. 2604–2616, Jun. 2020.
- [7] X. Wu, D. Hong, and D. Zhao, "Hyper-embedder: Learning a deep embedder for self-supervised hyperspectral dimensionality reduction," *IEEE Geosci. Remote Sens. Lett.*, vol. 19, 2022, Art. no. 5510605.
- [8] D. Wang, L. Zhuang, L. Gao, X. Sun, M. Huang, and A. Plaza, "BockNet: Blind-block reconstruction network with a guard window for hyperspectral anomaly detection," *IEEE Trans. Geosci. Remote Sens.*, vol. 61, 2023, Art. no. 5531916.
- [9] X. Shang et al., "Target-constrained interference-minimized band selection for hyperspectral target detection," *IEEE Trans. Geosci. Remote Sens.*, vol. 59, no. 7, pp. 6044–6064, Jul. 2021.
- [10] B. Asghari Beirami and M. Mokhtarzade, "Band grouping SuperPCA for feature extraction and extended morphological profile production from hyperspectral images," *IEEE Geosci. Remote Sens. Lett.*, vol. 17, no. 11, pp. 1953–1957, Nov. 2020.
- [11] J. Zhang, P. Zhang, B. Li, L. Jing, and T. Lv, "Semisupervised feature extraction based on collaborative label propagation for hyperspectral images," *IEEE Geosci. Remote Sens. Lett.*, vol. 17, no. 11, pp. 1958–1962, Nov. 2020.
- [12] B. Zhao, J. R. Sveinsson, M. O. Ulfarsson, and J. Chanussot, "Semi-supervised mixtures of factor analyzers feature extraction for hyperspectral images," *IEEE Geosci. Remote Sens. Lett.*, vol. 19, 2022, Art. no. 5500605.
- [13] M. Song, C. Yu, H. Xie, and C.-I. Chang, "Progressive band selection processing of hyperspectral image classification," *IEEE Geosci. Remote Sens. Lett.*, vol. 17, no. 10, pp. 1762–1766, Oct. 2020.
- [14] H. Yang, Q. Du, H. Su, and Y. Sheng, "An efficient method for supervised hyperspectral band selection," *IEEE Geosci. Remote Sens. Lett.*, vol. 8, no. 1, pp. 138–142, Jan. 2011.
- [15] M. Riedmann and E. J. Milton, "Supervised band selection for optimal use of data from airborne hyperspectral sensors," in *Proc. IEEE Int. Geosci. Remote Sens. Symp.*, Toulouse, France, 2003, pp. 1770–1772.
- [16] J. Feng, L. Jiao, F. Liu, T. Sun, and X. Zhang, "Mutual-information-based semi-supervised hyperspectral band selection with high discrimination high information and low redundancy," *IEEE Trans. Geosci. Remote Sens.*, vol. 53, no. 5, pp. 2956–2969, May 2015.
- [17] C.-I. Chang, Q. Du, T.-L. Sun, and M. L. G. Althouse, "A joint band prioritization and band-decorrelation approach to band selection for hyperspectral image classification," *IEEE Trans. Geosci. Remote Sens.*, vol. 37, no. 6, pp. 2631–2641, Nov. 1999.
- [18] B. Xu, X. Li, W. Hou, Y. Wang, and Y. Wei, "A similarity-based ranking method for hyperspectral band selection," *IEEE Trans. Geosci. Remote Sens.*, vol. 59, no. 11, pp. 9585–9599, Nov. 2021.
- [19] P. Gao, J. Wang, H. Zhang, and Z. Li, "Boltzmann entropy-based unsupervised band selection for hyperspectral image classification," *IEEE Geosci. Remote Sens. Lett.*, vol. 16, no. 3, pp. 462–466, Mar. 2019.
- [20] Y. Yuan, J. Lin, and Q. Wang, "Dual-clustering-based hyperspectral band selection by contextual analysis," *IEEE Trans. Geosci. Remote Sens.*, vol. 54, no. 3, pp. 1431–1445, Mar. 2016.
- [21] Y. Zhao, Y. Yuan, and Q. Wang, "Fast spectral clustering for unsupervised hyperspectral image classification," *Remote Sens.*, vol. 11, no. 4, Feb. 2019, Art. no. 399.
- [22] S. Li, Z. Wang, L. Fang, and Q. Li, "An efficient subspace partition method using curve fitting for hyperspectral band selection," *IEEE Geosci. Remote Sens. Lett.*, vol. 21, 2024, Art. no. 5501605.
- [23] Q. Wang, Q. Li, and X. Li, "Hyperspectral band selection via adaptive subspace partition strategy," *IEEE J. Sel. Topics Appl. Earth Observ. Remote Sens.*, vol. 12, no. 12, pp. 4940–4950, Dec. 2019.
- [24] S. Li, B. Peng, L. Fang, Q. Zhang, L. Cheng, and Q. Li, "Hyperspectral band selection via difference between intergroups," *IEEE Trans. Geosci. Remote Sens.*, vol. 61, 2023, Art. no. 5503310.
- [25] S. Jia, G. Tang, J. Zhu, and Q. Li, "A novel ranking-based clustering approach for hyperspectral band selection," *IEEE Trans. Geosci. Remote Sens.*, vol. 54, no. 1, pp. 88–102, Jan. 2016.
- [26] S. Li, Z. Liu, L. Fang, and Q. Li, "Block diagonal representation learning for hyperspectral band selection," *IEEE Trans. Geosci. Remote Sens.*, vol. 61, 2023, Art. no. 5509213.
- [27] Q. Wang, Q. Li, and X. Li, "A fast neighborhood grouping method for hyperspectral band selection," *IEEE Trans. Geosci. Remote Sens.*, vol. 59, no. 6, pp. 5028–5039, Jun. 2021.
- [28] W. Sun, L. Zhang, and B. Du, "A sparse self-representation method for band selection in hyperspectral imagery classification," in *Proc. 7th Workshop Hyperspectral Image Signal Process., Evol. Remote Sens.*, 2015, pp. 1–4.
- [29] W. Sun, L. Zhang, L. Zhang, and Y. M. Lai, "A dissimilarity-weighted sparse self-representation method for band selection in hyperspectral imagery classification," *IEEE J. Sel. Topics Appl. Earth Observ.*, vol. 9, no. 9, pp. 4374–4388, Sep. 2016.
- [30] S. Zhang et al., "Multiscale superpixel-based sparse representation for hyperspectral image classification," *Remote Sens.*, vol. 9, no. 2, Feb. 2017, Art. no. 139.
- [31] Q. Zhang et al., "Sparse representation based multi-sensor image fusion for multi-focus and multi-modality images: A review," *Inf. Fusion*, vol. 40, pp. 57–75, Mar. 2018.

- [32] P. Hu, X. Liu, Y. Cai, and Z. Cai, "Band selection of hyperspectral images using multi objective optimization-based sparse self-representation," *IEEE Geosci. Remote Sens. Lett.*, vol. 16, no. 3, pp. 452–456, Mar. 2019.
- [33] F. Li, P. Zhang, and L. Huchuan, "Unsupervised band selection of hyperspectral images via multi-dictionary sparse representation," *IEEE Access*, vol. 6, pp. 71632–71643, 2018.
- [34] S. Jia et al., "A multiscale superpixel-level group clustering framework for hyperspectral band selection," *IEEE Trans. Geosci. Remote Sens.*, vol. 60, 2022, Art. no. 5523418.
- [35] C. Yang, L. Bruzzone, H. Zhao, Y. Tan, and R. Guan, "Superpixel-based unsupervised band selection for classification of hyperspectral images," *IEEE Trans. Geosci. Remote Sens.*, vol. 56, no. 12, pp. 7230–7245, Dec. 2018.
- [36] Z. Feng, S. Yang, X. Wei, Q. Gao, and L. Jiao, "Regularized sparse band selection via learned pairwise agreement," *IEEE Access*, vol. 8, pp. 40096–40105, 2020.
- [37] W. Sun et al., "A multiscale spectral features graph fusion method for hyperspectral band selection," *IEEE Trans. Geosci. Remote Sens.*, vol. 60, 2022, Art. no. 5513712.
- [38] X. Wei, W. Zhu, B. Liao, and L. Cai, "Scalable one-pass self-representation learning for hyperspectral band selection," *IEEE Trans. Geosci. Remote Sens.*, vol. 57, no. 7, pp. 4360–4374, Jul. 2019.
- [39] Y. Zhang, X. Wang, X. Jiang, and Y. Zhou, "Marginalized graph self-representation for unsupervised hyperspectral band selection," *IEEE Trans. Geosci. Remote Sens.*, vol. 60, 2022, Art. no. 5516712.
- [40] J. Zhang et al., "Graph regularized spatial-spectral subspace clustering for hyperspectral band selection," *Neural Netw.*, vol. 153, no. 153, pp. 292–302, Sep. 2022.
- [41] X. Shang, C. Cui, and X. Sun, "Spectral-spatial hypergraph-regularized self-representation for hyperspectral band selection," *IEEE Geosci. Remote Sens. Lett.*, vol. 20, 2023, Art. no. 5504405.
- [42] W. Wang, Y. Qian, and Y. Y. Tang, "Hypergraph-regularized sparse NMF for hyperspectral unmixing," *IEEE J. Sel. Topic Appl. Earth Observ. Remote Sens.*, vol. 9, no. 2, pp. 681–694, Feb. 2016.
- [43] M.-Y. Liu, O. Tuzel, S. Ramalingam, and R. Chellappa, "Entropy rate superpixel segmentation," in *Proc. IEEE Conf. Comput. Vis. Pattern Recognit.*, Colorado Springs, CO, USA, 2011, pp. 20–25.
- [44] Y. Zhang, J. Wu, Z. Cai, and P. S. Yu, "Multi-view multi-label learning with sparse feature selection for image annotation," *IEEE Trans. Multimedia*, vol. 22, no. 11, pp. 2844–2857, Nov. 2020.
- [45] C. Sui et al., "Unsupervised hyperspectral band selection with multigraph integrated embedding and robust self-contained regression," *IEEE Trans. Geosci. Remote Sens.*, vol. 60, 2022, Art. no. 5504815.
- [46] Q. Wang, F. Zhang, and X. Li, "Optimal clustering framework for hyperspectral band selection," *IEEE Trans. Geosci. Remote Sens.*, vol. 56, no. 10, pp. 5910–5922, Oct. 2018.
- [47] S. Jia, Z. Lin, B. Deng, J. Zhu, and Q. Li, "Cascade superpixel regularized gabor feature fusion for hyperspectral image classification," *IEEE Trans. Neural Netw. Learn. Syst.*, vol. 31, no. 5, pp. 1638–1652, May 2020.
- [48] Y. Cai, Z. Zhang, X. Liu, and Z. Cai, "Efficient graph convolutional self-representation for band selection of hyperspectral image," *IEEE J. Sel. Topics Appl. Earth Observ. Remote Sens.*, vol. 13, pp. 4869–4880, 2020.
- [49] C. Tang et al., "Spatial and spectral structure preserved self-representation for unsupervised hyperspectral band selection," *IEEE Trans. Geosci. Remote Sens.*, vol. 61, 2023, Art. no. 5531413.
- [50] Y. Cai, X. Liu, and Z. Cai, "BS-nets: An end-to-end framework for band selection of hyperspectral image," *IEEE Trans. Geosci. Remote Sens.*, vol. 58, no. 3, pp. 1969–1984, Mar. 2020.
- [51] S. K. Roy, S. Das, T. Song, and B. Chanda, "DARecNet-BS: Unsupervised dual-attention reconstruction network for hyperspectral band selection," *IEEE Geosci. Remote Sens. Lett.*, vol. 18, no. 12, pp. 2152–2156, Dec. 2021.
- [52] H. Su, B. Zhao, Q. Du, and P. Du, "Kernel collaborative representation with local correlation features for hyperspectral image classification," *IEEE Trans. Geosci. Remote Sens.*, vol. 57, no. 2, pp. 1230–1241, Feb. 2019.
- [53] T. Cover and P. Hart, "Nearest neighbor pattern classification," *IEEE Trans. Inf. Theory*, vol. 13, no. 1, pp. 21–27, Jan. 1967.
- [54] M. Song, X. Shang, and C.-I. Chang, "3-D receiver operating characteristic analysis for hyperspectral image classification," *IEEE Trans. Geosci. Remote Sens.*, vol. 58, no. 11, pp. 8093–8115, Nov. 2020.
- [55] C.-I. Chang, Y.-M. Kuo, and P. F. Hu, "Unsupervised rate distortion function-based band subset selection for hyperspectral image classification," *IEEE Trans. Geosci. Remote Sens.*, vol. 61, 2023, Art. no. 5517218.



**Baijia Fu** received the B.S. degree in software engineering from Liaocheng University, Liaocheng, China, in 2022. She is currently working toward the M.S. degree in computer science and technology from Qingdao University, Qingdao, China.

Her research interests include machine learning and hyperspectral band selection.



**Xudong Sun** (Student Member, IEEE) received the B.E. degree in software engineering from Qingdao University, Qingdao, China, in 2016, and the M.S. degree in computer science and technology from Dalian Maritime University, Dalian, China, in 2020. He is currently working toward the Ph.D. degree in computer application technology at Dalian Maritime University.

His research interests include hyperspectral image processing, imaging science and photographic technology, and underwater robotics.



**Chuanyu Cui** received the B.S. degree in data science and software engineering from Qingdao University, Qingdao, China, in 2020, where he is currently working toward the M.S. degree in computer science and technology.

His research interests include deep learning and hyperspectral band selection.



**Jiahua Zhang** received the Ph.D. degree in cartography and remote sensing from the Institute of Remote Sensing Applications, Chinese Academy of Sciences, Beijing, China, in 1998.

From 1999 to 2001, he was a postdoctoral with the National Institute for Environmental Studies, Tsukuba, Japan. Since 2002, he has been a Professor with the Chinese Academy of Meteorological Sciences, Beijing. Since 2012, he has been a Full Professor with the Institute of Remote Sensing and Digital Earth, CAS, and a Professor with Qingdao University. He has published more than 200 peer-reviewed papers, 30 international conferences papers, and six books. His research interests include remote sensing and geosciences, vegetation dynamics, land use and land-cover classification, image processing, deep learning, and coastal environment remote sensing.



**Xiaodi Shang** (Member, IEEE) received the B.S. degree in software engineering from Qingdao University, Qingdao, China, in 2016, and the Ph.D. degree in computer application technology from Dalian Maritime University, Dalian, China, in 2022.

She is currently an Associate Professor with the College of Computer Science and Technology, Qingdao University. Her research interests include remote sensing and hyperspectral image processing.